Recovery of Salinity Gradient Energy in Desalination Plants by Reverse Electrodialysis

Accepted Manuscript

Desalination

13 August 2020

C. Tristán, M. Fallanza, R. Ibáñez, I. Ortiz*

Department of Chemical and Biomolecular Engineering, University of Cantabria,
Av. Los Castros 46, 39005 Santander, Spain.
*Corresponding author: ortizi@unican.es

ABSTRACT

Salinity gradient energy (SGE) capture by reverse electrodialysis (RED) is an emerging technology to advance the phaseout of conventional water-intensive energy sources in desalination industry. This paper assesses SGE recovery potential of an up-scaled RED system in seawater reverse osmosis (SWRO) desalination plants. Using a detailed RED system's model (i) we conducted a parametric evaluation of feed's concentration, feed's flow rate, and temperature to identify the optimal working conditions of an industrial-scale RED unit; (ii) we estimated SGE recovery of a RED plant in SWRO plants distributed worldwide, adopting a single-stage arrangement of the RED units; (iii) finally, to enhance energy yield, we examined different RED plant's layouts in a specific SWRO plant. The results underline the merits of this modelling tool to assist SGE-RED implementation in the utmost scenarios. Regarding RED plant's layout, findings reveal that the series-parallel arrangement of the RED units improves the power output and energy yield of the system but requires more RED units. Hence, a systematic evaluation through optimization of the hybrid process's configuration both at plant's scale and at RED unit's scale is needed to properly determine RED's SGE recovery potential from waste streams in SWRO plants.

Keywords: net power density; energy yield; plant layout; specific energy consumption; RED multi-scale model

1. INTRODUCTION

The rising water demand and the steady decline of conventional water resources [1] are hastening the use of unconventional ones, such as desalinated, re-used, and reclaimed water [1,2]. Over the period to 2040, the energy use in the water sector is projected to more than double, primarily driven by desalination. Even though desalination and water re-use met less than 1% of global water needs in 2016, these processes accounted for almost a quarter of total energy consumption in the water sector. By 2040, is expected to increase up to 4% of the water supply, but 60% of the water sector's energy consumption [3]. The high specific energy use hinders desalination widespread use and environmental sustainability, as this process is heavily reliant on fossil-fuel-based power sources. The most promising route foreseen is the shift to low-emissions off-grid renewable energy technology with little water requirements.

Salinity gradient, a clean and steady renewable energy source, can provide an integrated solution to the water-energy nexus challenge. Moving forward the gradual decarbonization of the desalination industry as it supports the phaseout of conventional water-intensive energy sources. Salinity gradient energy (SGE), or the Gibbs free energy, –released when two solutions of different concentration spontaneously mix–, is converted into useful work by the controlled mixing of the salinity gradient in engineered processes. The most promising process to harvest SGE, from those proposed so far, is reverse electrodialysis (RED) [4,5]. RED is an emerging electro-membrane technology that draws electric power from the chemical potential difference between two solutions by using ion-exchange membranes (IEMs).

RED has made noteworthy advances in fundamental-based studies, experimental investigations, and field demonstrations devoted to (i) stack design improvements, –IEMs (low electrical resistance, high permselectivity, profiled membranes), electrode systems

(electrode, electrode rinse solutions), spacers (ion-conductive spacers, novel designs)–; (ii) operational conditions –temperature, feed solutions' concentrations and composition, flow rate, flow modes, fouling issues–; and (iii) hybrid applications [6–8]. Jointly has led to remarkable progress in RED's performance ever since Pattle devised the process in the early '50s [9]. Over the last decades, power density, i.e. the power delivered per effective membrane's area, has grown from 0.05 W m^{-2} (reported in the pioneer experiments of Pattle) to 6.70 W m^{-2} recently realized by Daniilidis et al. mixing synthetic NaCl solutions mimicking fresh or brackish water (0.01 M) and concentrated brines (5 M) at a temperature of 60 °C [10]. Last research advances have stepped up RED Technology Readiness Level enabling the progress from lab-scale units [11,12] to up-scaled prototypes [13–17] and even pilot plants [18,19]

RED also opens up the chance to recover energy from abundant yet largely unused sources. as industrial effluents, which is a promising alternative to provide energy savings from an otherwise waste stream. Several authors have examined the energy retrieval from desalination's concentrate effluents [4,20–26], as well as secondary treated wastewater effluents [13,27–29]. Moreover, RED operation with high-salinity effluents delivers higher power densities than seawater/river water pairs extensively tested in prior works [10,27,30–35].

The development of RED process's modelling tools is also an extensive field of research [7,36]. **Table 1** collates some examples each one adopting different modelling approaches, e.g. lumped or distributed parameters models, simplified or semi-empirical models, considering different phenomena, e.g. mass transport across membranes, mass balance in the compartments and manifolds, electric phenomena, hydrodynamics, along with irreversibilities e.g. ohmic losses related to ionic conductivity of membranes (R_{IEM}) and solutions compartments (R_{sol}), non-ohmic losses relevant to concentration

polarization (ΔC_{BL}, R_{BL}) and concentration gradient along flow direction ($R_{\Delta C}$), uncontrolled mixing i.e. water and salt diffusion, due to non-ideal permselectivity of IEMs (α_{IEM}), hydrodynamic friction losses inside the channels (Δp), ohmic losses in the electrodic compartments (R_{blank}) and shortcut electric currents in the distribution manifolds (R_{man}), at different scales i.e. cell pair, stack and plant scale.

Simplified lumped parameters models consist of algebraic equations (for steady state problems) that synthesize into a small number of coefficients the behaviour of spatially dependent functions and use fitting parameters or empirical coefficients to account for non-idealities [37,38]; thus, requiring less computational effort at expense of reduced accuracy. While, semi-empirical distributed parameters models consider non-ideal phenomena and include algebraic phenomenological equations for salt and water fluxes through membranes, as well as mass balance differential equations to compute the variation of process parameters along the flow direction [34,35,39–46].

Trans-membrane mass transfer and hydrodynamics and the characterization of the Diffusion Boundary Layer (δ_{BL}, Sh) due to concentration polarization within compartments are described empirically or by Computational Fluid Dynamics (CFD) tools; IEMs can be modelled using macroscopic properties e.g. transport numbers or permselectivity, ohmic resistance, salt and water diffusivity, available from manufacturers or experimentally-accessible.

Table 1. Main features of some RED process simulation tools.

Reference	Domain	Mass balance	Mass transport		Non-ideal effects				Software
			Salt/Ions	Water	**Ω***	Non-Ω	α_{IEM}*	Δp	
Lacey (1980) [37]	1D	C_{bulk}	J_{cond}	NA	$R_{sol}(C,T)$ R_{IEM}	$R_{BL}(\Delta C_{BL})$ ΔC_{BL} (δ_{BL}*)	f(C, T)	sol: sp*	NR
Braun (2009) [38]	1D	C_{bulk}	J_{cond}	NA	$R_{sol}(C,T)$ R_{IEM} (δ_{IEM})	$R_{BL}(\Delta C_{BL})$ ΔC_{BL} (δ_{BL} Cst.)	Cst.	NA	TK-Solver
Veerman et al. (2011) [39]	1D	C_{bulk} (x) Q(x)	J_{cond} (x) J_{diff} (x)	J_{osm} (x)	$R_{sol}(C)$ R_{IEM}	NA	Cst.	stack*	Berkeley Madonna
Tedesco et al. (2015) [40]	1D + 3D (CFD)	C_{bulk} (x) C_{man} Q(x) Q_{man}	J_{cond} (x) J_{diff} (x)	J_{eosm} (x) J_{osm} (x)	$R_{sol}(C,T)$ $R_{man}(C, T)$ R_{IEM} (C,T) R_{blank}	$\Delta C_{BL}(x)$ (Sh**)	f(C, T)	sol: sp*	gPROMS
Tedesco et al. (2015) [41]	2D + 3D (CFD)	C_{bulk} (x,y) C_{man} Q(x,y) Q_{man}	J_{cond} (x,y) J_{diff} (x,y)	J_{eosm} (x,y) J_{osm} (x,y)	$R_{sol}(C,T)$ $R_{man}(C, T)$ R_{IEM} R_{blank}	$\Delta C_{BL}(x)$ (Sh**)	f(C, T)	sol: sp*	gPROMS
Pawlowski et al. (2016) [42]	1D + 3D (CFD)	C_{bulk} (x) Q(x)	J_{cond} (x)	NA	$R_{sol}(C,T)$ R_{IEM} (C) R_{blank}	$\Delta C_{BL}(x)$ (Sh**)	NA	sol: sp, pm**	OpenFOAM
La Cerva et al. (2017) [43]	1D + 3D (CFD)	C_{bulk} (x) Q(x)	J_{cond} (x) J_{diff} (x)	J_{eosm} (x) J_{osm} (x)	$R_{sol}(C,T)$ R_{IEM} (C) R_{blank}	$\Delta C_{BL}(x)$ (Sh**)	Cst.	$p_{sol}(x)$ sol: sp, pm** man	Excel G-95 Fortran gPROMS
Ortiz-Imedio et al. (2019) [34]	1D	C_{bulk} (x) Q(x)	J_{cond} (x) J_{diff} (x)	J_{osm} (x)	$R_{sol}(C,T)$ R_{IEM}	R_{BL} (x)* $R_{\Delta C}$ (x)	Cst.	NA	Aspen Custom Modeler
Ortega-Delgado et al. (2019) [44]	1D + 3D (CFD)	C_{bulk} (x) Q(x)	J_{cond} (x) J_{diff} (x)	J_{eosm} (x) J_{osm} (x)	$R_{sol}(C, T)$ R_{IEM} (C, T) R_{blank}	$\Delta C_{BL}(x)$ (Sh**)	f(C, T)	sol: sp**	Engineering Equation Solver (EES)

Gomez-Coma et al. (2019) [45]	1D	C_{bulk} (x) Q(x)	J_{cond} (x) J_{diff} (x)	J_{osm} (x)	R_{sol} (C,T) R_{IEM} (C)	R_{BL} (x)* $R_{\Delta C}$ (x)	Cst.	NA	Aspen Custom Modeler
Ortiz-Martinez et al. (2020) [35]	1D	C_{bulk} (x) Q(x)	J_{cond} (x) J_{diff} (x)	J_{osm} (x)	R_{sol} (C,T) R_{IEM}	R_{BL} (x)* $R_{\Delta C}$ (x)	Cst.	stack*	Aspen Custom Modeler
Culcasi et al. (2020) [46]	1D + 3D (CFD)	C_{bulk} (x) C_{man} Q(x) Q_{man}	J_{cond} (x) J_{diff} (x)	J_{eosm} (x) J_{osm} (x)	R_{sol} (C,T) R_{man} (C,T) R_{IEM} (C) R_{blank}	ΔC_{BL}(x) (Sh**)	f(C)	NA	gPROMS
This work	1D	C_{bulk} (x) Q(x)	J_{cond} (x) J_{diff} (x)	J_{osm} (x)	R_{sol} (C, T) R_{IEM} (T)	R_{BL} (x)* $R_{\Delta C}$ (x)	Cst.	p_{sol}(x) sol: sp*	Aspen Custom Modeler Aspen Plus

sol: concentrate or diluate compartment; man: manifolds; sp: spacer-filled; pm: profiled membrane; BL: Boundary Layer; δ: thickness; Sh: Sherwood number; ΔC_{BL}: Concentration gradient in the BL; ΔC: Concentration gradient in the bulk along channels' length; R_{blank}: electrode system's losses; *Experimental or empirical correlation; **CFD: Computational Fluid Dynamics;

Ortiz-Imedio et al. [34] building on Veerman et al. approach developed a comprehensive modelling tool that predicts the performance of a RED unit and assists in the selection of the optimum operating conditions in diverse scenarios The model has been extensively validated with lab-scale experimental data in several works [27,34,35,45], proving it as a robust and accurate simulation tool. Gomez-Coma et al. [47] extended the previous model to include the influence of solutions' ionic composition (concentration and presence of multivalent ions) on RED performance through empirical correlations of IEMs' resistance –derived from electrochemical impedance spectroscopy (EIS) measurements of commercial IEMs– as a function of concentration and ionic composition of feed solutions. The validated model can accurately predict RED performance over a wide range of feeds' concentrations and compositions relevant to real scenarios for RED implementation. Ortiz-Martinez et al. model [35] starting from Ortiz-Imedio et al. approach computes also pressure drops in the fluid compartments and the related pumping power cost to identify the optimum diluate's flow rate and concentration concerning the net power output of the RED unit. In this work, to expand feed temperature's and feed concentration's influence on RED performance, the Ortiz-Imedio et al.'s model has been updated to consider the solutions' physical and thermodynamic properties variation along the main flow direction, as well as solutions' temperature influence on membrane resistance. The distributed pressure drops in the RED stack's compartments and the required pumping power has been also considered, to compute the net power output of each RED unit.

So far, most of the reported studies in the open literature investigate the RED process as an independent unit operation, focusing primarily on improving the power density and the conversion efficiency of RED but few on the operation of multi-stage RED units arrangements in real operational environments to improve the energy fraction recovered from SGE [15,23,40,48–50].

Using the upgraded RED mathematical model previously developed in our research group [34], this paper aims to assess the technical potential of an up-scale SGE-RED system under several operational conditions determined by site-specific conditions representative of SWRO desalination plants in different worldwide locations.

The evaluation of (i) a stand-alone RED stack's performance; (ii) the actual power and energy attainable with an up-scaled SGE-RED process in different worldwide SWRO desalination plants and (iii) different SGE-RED plant's hydraulic arrangements of the RED units to seek well-balanced between maximum net power density and energy recovery, will contribute to bridging the gap between the maximum extractable work and actual power output of SGE-RED in the selected SWRO desalination plant scenarios.

2. METHODS

The analysis of the stand-alone RED unit and the SGE-RED plant was performed in the process simulation software Aspen Plus® V11 (AspenTech) [51] with the user-defined RED stack model implemented in Aspen Custom Modeler® V11 (AspenTech) [52]. All simulations refer to a commercial RED unit (Fumatech GmbH®, Germany), with a number of cell pairs (cp) representative of industrial-scale stacks (**Table 2**) fixing the minimum permselectivity and areal resistance of IEMs as reported by Fumatech (**Table 3**).

Table 2. Parameters of the commercial RED stack.

Number of cell pairs N_{cp}	**HC and LC compartments' dimensions**		
	Length L (m)	**Width b (m)**	**Height[a] δ_{sp} (μm)**
1000	0.383	0.456	270

Spacer's porosity ε = 82.5%

[a]Inter-membrane distance assumed equal to the spacer's thickness

2.1. SGE-RED model

The SGE-RED system's model is a nested structure hierarchized as follows: (i) at the lowest scale is the cell pair, the repeating unit in a RED pile, made up of a cation- and an anion-exchange membrane and two adjacent spacer-filled compartments alternatively flushed with concentrate (HC) and diluate (LC) feed streams; (ii) at the intermediate scale is the RED unit, the whole set of cell pairs stacked in series, which is modelled as an analogous DC circuit; and (iii) at the uttermost scale is the SGE-RED plant defined by different RED stacks' arrangements giving different plant layouts (**Fig. 1**).

The cell pair model, thoroughly described in Ortiz-Imedio et al. work [34] and Supplementary material, is a system of algebraic and differential equations defining mass balances, transport phenomena, solutions' thermodynamics, and electrical parameters within the cell pair. The thermodynamic and electrical equations determine the cell pair's potential and resistance (E_{cp} and R_{cp} respectively, **Fig. 1**), and the electric current and electric potential of the stack (I_{stack} and E_{stack}, **Fig. 1**). The differential mass balance equations for each ion in the diluate and the concentrate solution, linked by mass transfer equations, define the bulk ionic concentration and flow rate distributions along the channels (C(x) and Q(x), **Fig. 1**). The transport equations provide the mass flux of ions – electromigration of counter-ions and diffusion of co-ions ($J_{cond}(x)$ and $J_{diff}(x)$, **Fig. 1**)– and water –osmosis ($J_{osm}(x)$, **Fig. 1**)– through membranes.

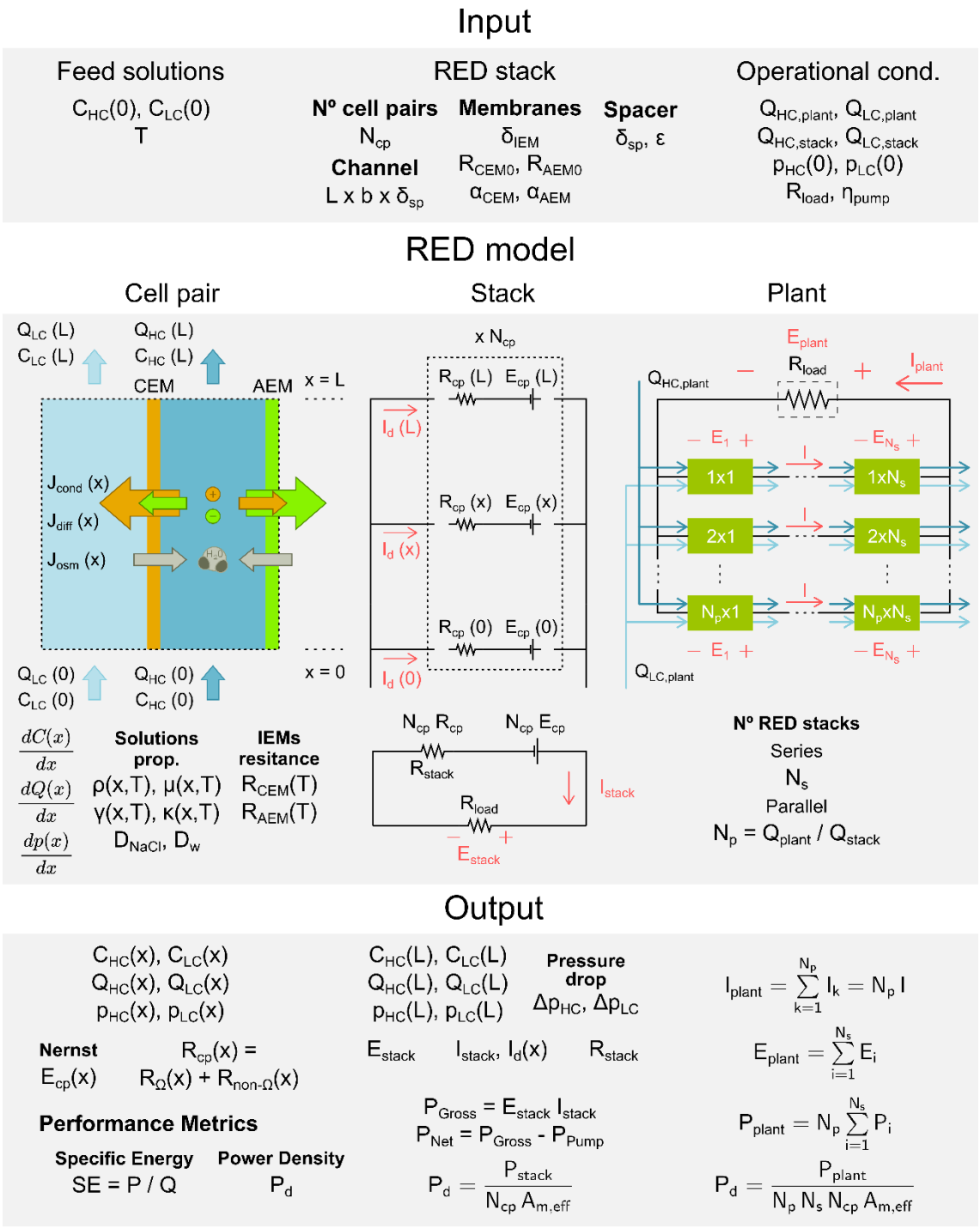

Figure 1. Flowchart of the RED's simulation tool.

The RED's model was numerically solved over the channel's domain, which was discretized along the main flow direction (1-D distributed model). Each discretized element represents a branch of the RED stack's equivalent DC circuit, with passive (i.e. ohmic R_{Ω} and non-ohmic resistances $R_{non\text{-}\Omega}$, **Fig. 1**) and active (i.e. electromotive force

(e.m.f.) of a cell pair equal to the sum of CEM's and AEM's electric potential, (E_{cp}, **Fig. 1**) elements in series.

The validated RED stack model [27,34,35,45] detailed in Supplementary material, was updated as follows:

- To consider feed temperature's and feed concentration's influence, the RED stack model was reworked to account for solutions' physical (i.e. density ρ(x,T), viscosity μ(x,T), **Fig. 1**) and thermodynamic (i.e. activity coefficients γ(x,T), **Fig. 1**) properties variation along the main flow direction with Aspen's ELECNRTL thermodynamic package.
- Distributed pressure drops in the RED stack' spacer-filled compartments and the required pumping power was also considered, to compute the net power output of each RED unit.
- Solutions' temperature influence on membranes' resistance was also included and modelled through an empirical equation from Mehdizadeh et al. work [53].

The main simplifying assumptions adopted are detailed in Supplementary material.

Table 3. Reference properties of membranes based on manufacturer specifications (Fumatech GmbH®, Germany).

Membrane	**Areal Resistance R_{IEM0} (Ω cm^2)[a]**	**Permselectivity α_{IEM} (%)[b]**	**Thickness dry δ_{IEM} (μm)**	**Active area $A_{m,eff}$ (m^2)[c]**
fumasep® FKS-50 CEM	1.8–2.5	97–99	50	0.175
fumasep® FAS-50 AEM	0.6–1.5	92–96	50	0.175

[a]Measured in 0.5 M NaCl at 25 °C
[b]Measured in 0.1/0.5 mol kg^{-1} KCl at 25°C
[c]$A_{m,eff}$ = b L (**Table 1**)

2.2. Site-specific scenarios: SWRO desalination plants

The RED system's energy retrieved from RO's brine effluent was estimated using reported data (summarized in **Table 4**) from six large-size SWRO desalination plants [54–58].

Table 4. Main features of seawater reverse osmosis desalination plants to assess SGE-RED plant's power and energy supply [54–58].

SWRO desalination plant	Recovery Rate		SEC[a] (kWh m^{-3})	Product water (m^3 day^{-1})	1st pass RO brine	
	1st pass	2nd pass			(m^3 m^{-3})[b]	(M)
SingSpring	0.45	0.90	4.1	136,400	1.33	0.98
Sydney	0.45	0.86	3.9	250,000	1.38	1.13
Fukuoka	0.60	0.85	5.5	50,000	0.76	1.49
Barcelona (Llobregat)	0.45	0.85	4.2	200,000	1.39	1.23
Sadara	0.45	0.90	4.4	148,800	1.33	1.40
Carlsbad[a]	0.45	0.85 0.85 0.90	3.6	190,000	1.24	1.14

Overall RO configuration: Partial two-pass excepting Carlsbad (split partial tow-pass with a 4-stage cascade configuration).
[a]SEC: Specific energy consumption, i.e. energy consumption per m^3 of desalted water. Including intake/outtake, pre-treatment, RO and post-treatment processes as well as energy recovery device.
[b]Brine volume per cubic meter of product water.

All desalination plants use a partial two-pass RO configuration (**Fig. 2a**) except Carlsbad, which uses a four-stage cascade configuration (**Fig. 2b**), where the 1st and 2nd RO stages comprise the Split-Partial Second Pass stage (SPSP) –the 2nd pass treats a smaller, but more saline 1st RO pass's permeate than a conventional partial two-pass system– and the 3rd and 4th RO stages the conventional full two-pass RO stage.

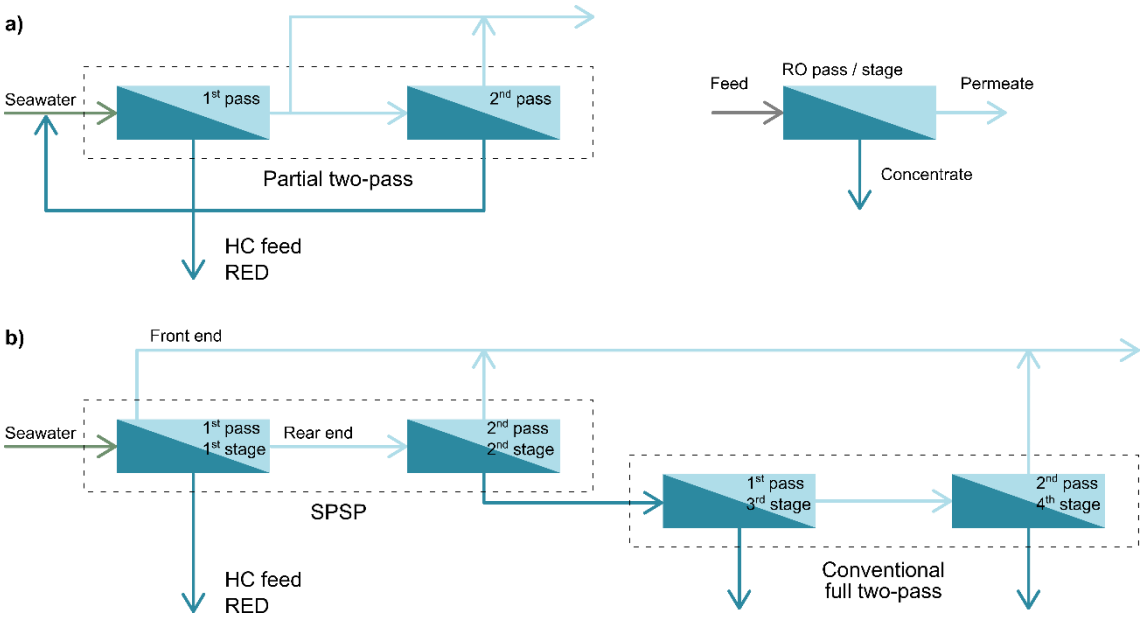

Figure 2. Overall RO configuration of SWRO desalination plants: a) Partial-two pass and b) Four-stage cascade (Carlsbad desalination plant).

The 1st RO pass brine effluent is fed to the high-saline compartments (HC feed RED, **Fig. 2**) of the RED unit. We estimated the volume and concentration of the 1st RO pass concentrate effluent solving mass balance for each SWRO plant considering the overall RO configuration and the water recovery rate, i.e. the volume of desalted water to feed water's volume, of the desalination plant, as well as the product water's and feed seawater's salinity.

The SGE recovery potential was determined considering: (i) the salinity gradient exergy content (Gibbs free energy of mixing), and (ii) the net energy and net power density output of the SGE-RED system.

3. RESULTS AND DISCUSSION

First, using the mathematical model described earlier, we conduct a parametric evaluation of the main operational variables influencing the RED unit's power generation. Afterwards, the study is extended to the SGE-RED plant's performance under different operational conditions relevant to site-specific conditions to assess the technical potential of SGE-RED process in real operational environments, specifically, six SWRO desalination plants distributed worldwide. Finally, we examine how different SGE-RED plant layouts in a specific SWRO desalination plant could improve the overall power supply and energy recovery of the RED system.

3.1. Stand-alone RED stack performance

This section surveys a parametric analysis of site-constrained operating variables –salinity and temperature of RED's inlet streams–, and the ones open for design, –feed's flow rate and, to some extent, the diluate's concentration– on RED unit's power generation and energy recovery, to determine the optimum working conditions to adopt in the SGE-RED plant. **Table 5** summarizes the operating conditions set in each parametric assessment.

Table 5. Operational conditions of the stand-alone RED stack unit: inlet's concentration, flow rate and temperature.

Operation variable	**C_{HC} (M)**	**C_{LC} (mM)**	**T (°C)**	**v (cm s^{-1})**
Concentration	2.0–0.5	500–0.1	24	3.0
Flow rate (linear cross-flow velocity)	1.0	20	24	0.3–3.0
Temperature and diluate's flow rate	1.0	20	10–30	0.7–2.0 (v_{HC}:v_{LC} = 0.6, fixed)

Co-current flow distribution

3.1.1. Influence of feed solutions' concentration

Fig. 3 shows the RED unit's gross and net power density output under varying concentration of both concentrate (2.0–0.5 M) and diluate ($0.5–1\cdot10^{-4}$ M) feed solutions working with the maximum flow rate i.e. 3.0 cm s^{-1} and 24 °C. The concentration ranges were set based on representative salinities of streams in membrane-based desalination processes.

The inlet solutions' concentration not only defines the potential SGE available for conversion, but also the electromotive force (e.m.f.) and the internal resistance of the RED stack. Prior research generally confirms that growing concentrate solution's concentrations gradually enhance the power produced, which is mainly related to the larger concentrate to diluate activity's ratio that increase the driving force [33,44,59,60]. As **Fig. 3** infers, the power density follows an upward trend over high-saline solution's concentration range, regardless of diluate's salinity.

Unlike concentrate solution's, the diluate's concentration is a major factor in the relative influence of RED's e.m.f. and internal resistance on the actual power output of the system, as **Fig. 3** reveals. The use of solutions with very low conductivity undermines RED's power output [35], since, the RED stack's resistance rise outweighs the gain in driving force, i.e. the e.m.f. By contrast, as diluate's and concentrate's concentration equals each other, the salinity gradient nears zero, and so does the driving force, despite the internal resistance decline. Consequently, for each concentrate solution there is a local diluate's concentration that maximizes the power density of the RED stack. The net power density peaks to 0.46 W m^{-2} per cell pair (when mixing a 23 mM / 0.5 M NaCl solutions) and increases up to 4.05 W m^{-2} per cell pair (when mixing 59 mM / 2.0 M NaCl solutions). The diluate's concentration range, that defines the optimal power density region i.e. ~80%

the maximum net power density, widens as concentrate's salinity increases, moving from 0.040–0.012 M, when seawater (0.05 M) is used as concentrate stream, to 0.163–0.017 M, when the RED unit operates with high-saline brines (2.0 M).

The solutions' thermodynamic and physical properties are also affected by concentration. As the feed concentration increase so does the solutions' viscosity –e.g. ~14% growth when concentrate's salinity is quadrupled (from 0.5 M to 2.0 M) and a ~4% decline when diluate's concentration falls from 0.5 M to $1 \cdot 10^{-4}$ M–, leading to slightly higher pressure drops within the channels. Even so, the pump work remains roughly constant over low- and high-solution concentration span; Indeed, under optimum diluate's concentration, the pumping power demand increases by about 7% when concentrate's concentration is four folded from 0.5 to 2.0 M; however, the gross power gain greatly offset this increment. The pump power makes up 74.7% of the gross power produced at 0.5 M ($P_{d,gross}$ = 1.83 W m^2 per cell pair) and drops to 26.5% at 2.0 M ($P_{d,gross}$ = 5.52 W m^2 per cell pair).

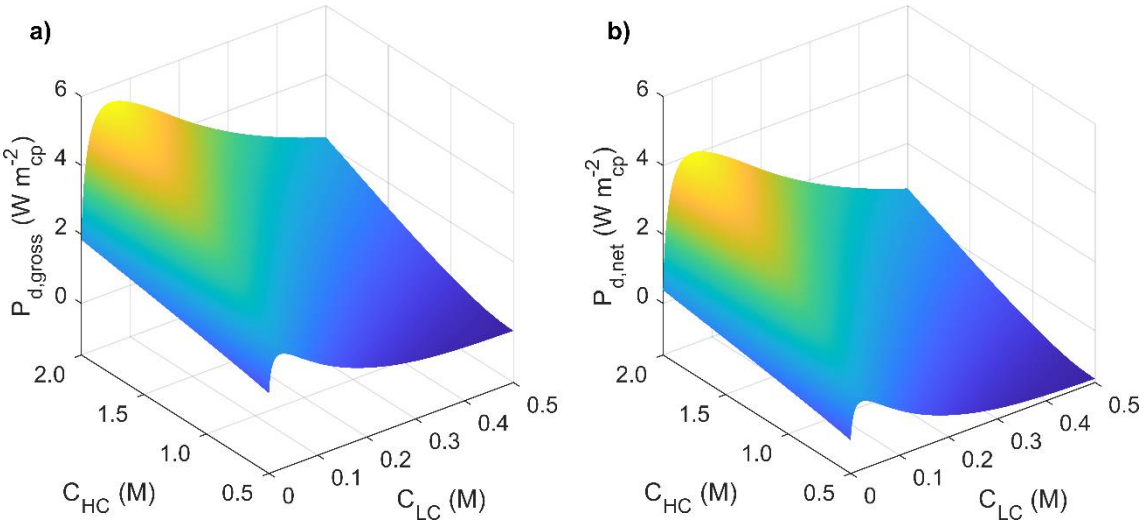

Figure 3. Stand-alone RED stack: a) gross and b) net power density as a function the concentrate (HC) and diluate (LC) inlet concentration. Working conditions: $v_{HC} = v_{LC}$ = 3.0 cm s^{-1}, $T_{HC} = T_{LC}$ = 24 °C.

3.1.2. Influence of feed solutions' flow rate

The flow rate of both the concentrate and the diluate feed solutions was varied from 1.33 $m^3 h^{-1}$ up to the upper limit specified by the manufacturer, i.e. 13.3 $m^3 h^{-1}$, –corresponding to a solution's linear velocity range in each compartment of 0.3–3.0 cm s^{-1}– at a fixed feed's concentration and temperature to determine the concentrate to diluate flow rate ratio that gives the maximum net power density.

High flow rates of the concentrate and the diluate streams keep uniform the concentration differences across membranes and improve fluid mixing in the compartments. Hence, as **Fig. 4a** reveals, the gross power density rises monotonically with feed's flow rate until the plateau region is reached, where the low conductivity of the diluate solution offsets the modest e.m.f. growth. Concurrently, improved fluid mixing in the compartments reduces concentration polarization phenomena, and concentration gradient over the channel's length, i.e. the non-ohmic contribution, enhancing the gross power output of the system; however, it also gives rise to higher hydrodynamic loss that reduces the RED unit's net power output [35]. Thereby, for a given cell configuration and feed's concentration, exists an optimal flow regime where the net power output peaks.

Notably, as **Fig. 4** shows, the power delivered is more sensitive to diluate's flow rate variations than concentrate ones. The gross power density levels off earlier when the RED unit works with larger concentrate's flow rate at a specific diluate's velocity. Given pump power consumption is a quadratic function of flow rate, under fixed diluate's flow velocity, the maximum net power density is reached at lower concentrate's linear velocity. Even more, the optimal concentrate to diluate linear velocity ratio, v_{HC}:v_{LC}, is ~0.6, (v_{HC} = 1.0 cm s^{-1} and v_{LC} = 1.7 cm s^{-1}). Under this flow regime, the maximum net power density equals 2.42 W m^{-2} per cell pair corresponding to a gross power density of 2.72 W m^{-2} per cell pair.

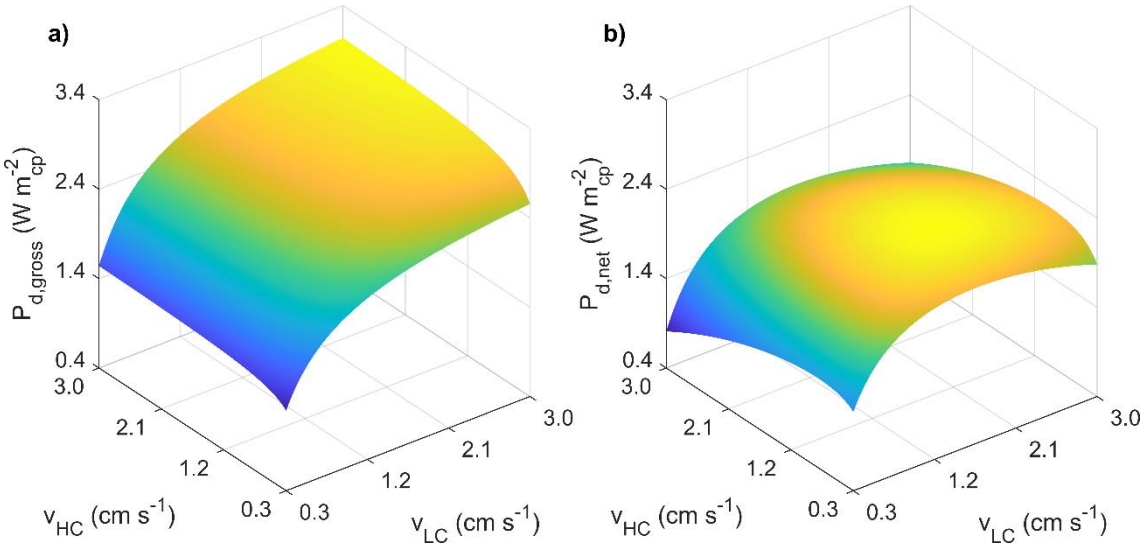

Figure 4. Stand-alone RED stack: a) gross and b) net power density as a function the concentrate (HC) and diluate (LC) linear cross-flow velocity. Working conditions: C_{HC} / C_{LC} = 1.0/0.02 M, T_{HC} = T_{LC} = 24 °C.

3.1.3. Influence of feed solutions' temperature

The RED's performance is not only sensitive to inlet concentration and flow rates, but also solutions' temperature. Given feed's temperature is not at designer disposal, as it depends on site-specific conditions, we evaluate the RED unit's performance in the temperature range set according to reported seasonal records in different worldwide locations. The diluate's flow rate was varied within the optimal range, i.e. 0.7–2.0 cm s^{-1}, fixing the optimal concentrate to diluate linear velocity ratio to 0.6.

Working in warmer conditions enhances the performance of the RED stack due to the e.m.f. increase and the RED stack's resistance decline stemmed from the higher conductivity of solutions and IEMs [33,44,53,61]. As expected, the gross power density rises with temperature (**Fig. 5a**); however, feed's flow rate affects differently power density's sensitivity to temperature. The gross power density rises linearly at a rate of 3.3% per °C at v_{LC} = 0.7 cm s^{-1} and moves up to 5.2% per °C at v_{LC} = 2.0 cm s^{-1}, leading

to an overall gross power increase from 1.47 W m^{-2} to 1.90 W m^{-2} and from 2.20 W m^{-2} to 3.20 W m^{-2}, respectively, when temperature is tripled from 10 °C to 30 °C.

Concurrently, the pumping power progressively falls with temperature as the feed solutions turn less viscous in warmer conditions. The viscosity of both streams decreased by ~37% when temperature goes up from 10 °C to 30 °C. Interestingly, the influence of solutions' viscosity on net power density is more relevant with rising flow rates, as the pumping power is proportional to viscosity and increases quadratically with flow rate. Thus, the optimal diluate's linear velocity gradually increases from 1.20 cm s^{-1} at 10 °C ($P_{d,net}$ = 1.53 W m^{-2} per cell pair) up to 1.96 cm s^{-1} when solutions warm up to 30 °C ($P_{d,net}$ = 2.84 W m^{-2} per cell pair).

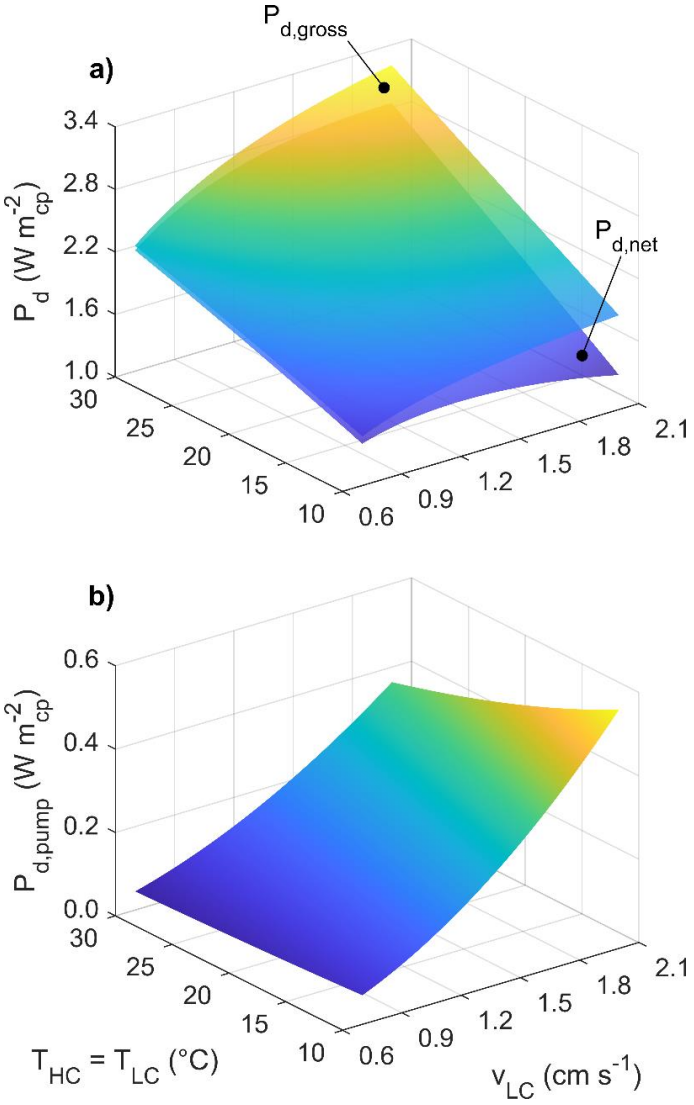

Figure 5. Stand-alone RED stack: a) gross and net power density and b) pump power density as a function of the diluate's linear cross-flow velocity and temperature (assumed equal for the HC and LC streams). Working conditions: C_{HC} / C_{LC} = 1.0/0.02 M, v_{HC}: v_{LC} = 0.6.

3.2. SGE-RED energy recovery in site-specific scenarios

This section will focus on the actual generation of SGE-RED process in globally distributed SWRO desalination plants. We quantified the energy recovery and power production of the SGE-RED plant in each scenario, under optimal working conditions of the product-scale RED stack (**Table 6**) according to the parametric evaluations discussed earlier.

The SGE recovery potential in each location was estimated based on the maximum extractable work given by the Gibbs free energy of mixing, and the actual net specific energy and net power density of the RED system through simulation. The SGE-RED plant's net supply was determined (i) assuming a parallel hydraulic configuration of the RED units i.e. the concentrate and diluate streams are evenly split between the RED stacks; (ii) considering the SWRO concentrate effluent was fully fed to the high-salinity compartments of the RED units; (iii) setting the operating temperature according to location and assumed equal for both the concentrate and the diluate streams; (iv) assuming unlimited availability of diluate's feed volume for energy conversion.

Table 6. SGE-RED plant's operational conditions for every RED unit in the SGE-RED plant according to location, i.e. SWRO desalination plant.

SWRO desalination plant	**C (M)**		**v (cm s^{-1})[b]**		**T (°C)**
	HC[a]	**LC[b]**	**HC**	**LC**	
SingSpring	0.98	0.035	1.30	2.23	31
Sydney	1.13	0.040	1.02	1.79	20
Fukuoka	1.49	0.050	1.13	1.95	20
Barcelona (Llobregat)	1.23	0.045	1.02	1.79	19
Sadara	1.40	0.045	1.30	2.22	27
Carlsbad	1.14	0.045	1.02	1.73	18

[a]Equal to 1st pass RO brine's concentration.
[b]Optimal net power density working conditions determined with RED's model

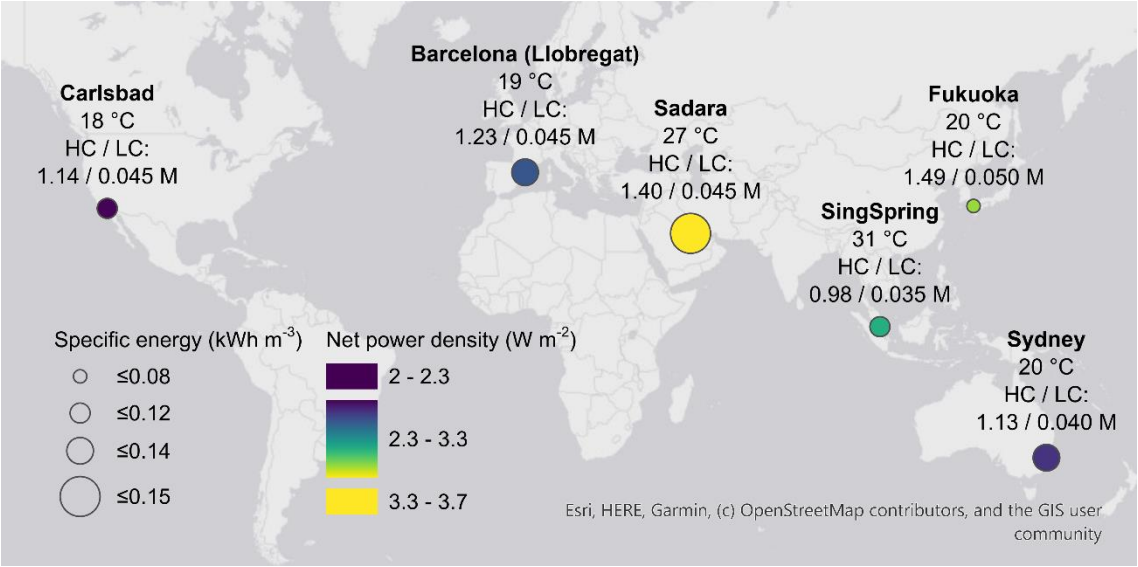

Figure 6. Site-specific scenarios: net specific energy and net power density delivered by SGE-RED plant. Feed's solution concentration and temperature in each location are also displayed. Note: the bubble size denotes the net specific energy output, while the colorbar the net power density supplied in each SWRO desalination plant's location.

Fig. 6 depicts the net power density and the net specific energy, –net energy per m^3 of desalted water–, delivered by the RED system in each scenario. The bubble's size scales with the net specific energy, while the graduated color scale refers to the net power density. As outlined earlier, the concentration and temperature of the inlet streams, substantially affect the net power density of the system. The upper range of (i) brine's concentration, found in Sadara and Fukuoka desalination plants effluents, and (ii) temperature (SingSpring and Sadara), provides the highest power densities (yellow to green hues in the map). However, the feed's volume availability bounds the potential specific energy supply of the SGE-RED plant. For instance, the scarce brine's volume available in Fukuoka plant (0.76 m^3 m^{-3}, owing to the high recovery rate i.e. the volume of water desalted per volume of seawater withdrawn, of 60%, **Table 4**) greatly hampers the energy capacity of the SGE-RED plant, despite the high net power density delivered in this scenario. Similarly happens with SingSpring's operational conditions. In contrast, Barcelona and Sadara desalination plants supply almost twice Fukuoka brine effluent's

volume to the SGE-RED plant, leading to a 65% and 77% increase in the net specific energy, (from 0.08 kWh m^{-3} to 0.13 kWh m^{-3} and 0.15 kWh m^{-3}) respectively. Overall, Sadara's scenario holds the best-operating conditions, i.e. high brine's concentration and warm conditions combined with large brine's volume. The worst-case scenario is found in Carlsbad, where the soft temperature together with the limited concentrate's volume hinder SGE-RED plant's net power density and net specific energy capacity, followed by Sydney's plant, as it has slightly more brine's volume available for conversion.

The mixing free energy per unit volume of desalted water sets the upper energy savings to drive desalination. Theoretically, if salinity gradient's chemical energy is completely converted into useful work, the SGE-RED plant's supply could cut by 22% to 47% the SWRO plant's energy needs. However, SGE-RED plant's net energy supply differs from the theoretical maximum extractable work, provided (i) RED's energy conversion is irreversible, and (ii) a great fraction of the exergy input remains untapped. Thus, SGE-RED plant's net energy output could only meet ~3% of the SWRO plant's demand, aside from Fukuoka scenario –which features the highest SEC along with the lowest net specific energy–, where the energy's share is halved.

Even so, as was stated before, only a small portion of the exergy input is retrieved for conversion, resulting in net energy yield of the SGE-RED plant, i.e. the exergy fraction converted to useful work, of 7%–8%. Unused SGE leaving the RED system can be further recovered by additional downstream RED units installed in the plant, thus narrowing the gap between the theoretical thermodynamic limit and the overall energy harnessed by the SGE-RED plant. These results denote the SGE-RED plant layout should be carefully revised to make more efficient use of these waste streams, increasing the energy share delivered to the SWRO plant.

3.3. SGE-RED plant layouts

The different RED unit's arrangements (depicted in **Fig. 7**) were analyzed in Barcelona SWRO desalination plant, as it gathers a good balance of power density, energy potential, and source availability.

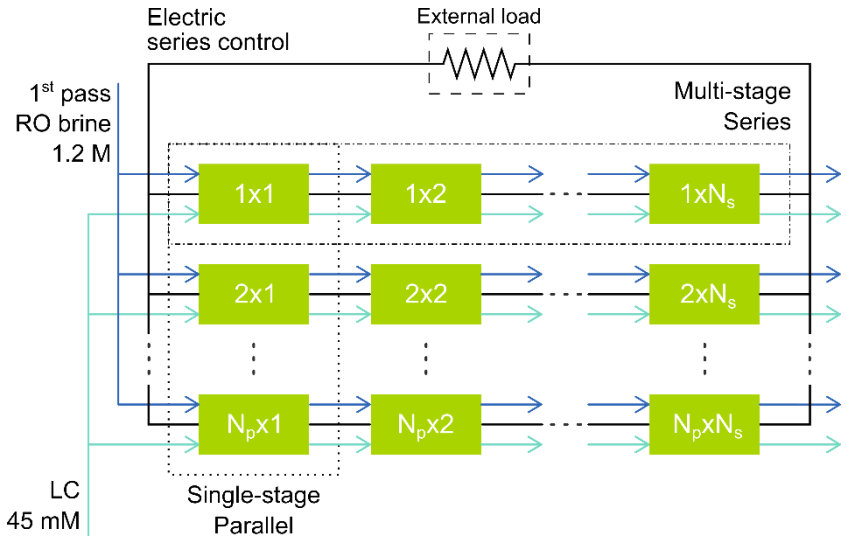

Figure 7. SGE-RED plant's layout: scheme of the RED unit's hydraulic and electric network with N_p units in parallel and N_s stacks in series.

Single-stage, parallel arrangement. Already assessed in the former section. The incoming concentrate and diluate streams are evenly fed to the RED stacks recovering SGE in one pass (**Fig. 7**, Single-stage). All the RED units work with the same operating conditions reported earlier in **Table 6**. The maximum number of RED units in the parallel arrangement is given by the SWRO's brine flow rate divided by the concentrate inlet's flow rate in each stack, yielding 2560 RED units of 1000 cell pairs and 0.175 m^2 effective area per membrane.

Since all the RED units work with the maximum SGE, the power delivered by each stack –and the overall plant's power output–, is greater ($P_{d,net}$ = 2.56 W m^{-2}, P_{net} = 1.15 MW); however, a large SGE fraction exits the RED units unused (~73%), reducing the overall energy efficiency of the SGE-RED plant to ~7%. The RED parallel arrangement's net energy output (0.14 kWh m^{-3}) could roughly meet 3% of the SWRO plant's SEC.

Multi-stage, series arrangement. SGE is harnessed in consecutive passes. In this configuration, the RED unit's concentrate and diluate outlet streams are directly fed to the next stack in the series setup (**Fig. 7**, Multi-stage). The 1st unit operates with equal conditions as the RED units in the parallel arrangement (**Table 6**), the remainder units run with equal electric current as the 1st stack (series electric control).

The series network recovers a greater fraction of the SGE for conversion, thus enhancing the SGE-RED plant's energy yield that nearly triples (~20%) when installing five RED units in series (net specific energy, 0.37 kWh m^{-3}). Even so, the series SGE-RED system's power production and reclaimed volume capacity are lower compared to the parallel configuration. While the SGE recovery increase, the driving force decline over each downstream series stage causes a dramatic decline in the overall net power density (from 2.56 W m^{-2} to 1.11 W m^{-2}) owing to the longer equivalent flow path of the series arrangement compared to the parallel one. Moreover, the gross power density of the last RED unit is unable to overcome the pump consumption resulting in negative net power density, that further reduces the overall net power and net energy output of the series network, which peaks at the fifth stage.

Series-parallel arrangement. The combination of the foregoing series and parallel arrangements offers a trade-off between the power output –achieved in the parallel network–, and the energy yield –delivered in the series one–.

The maximum net power of the series-parallel network (3.10 MW) almost tripled the power output of the parallel arrangement (**Fig. 8b**) with an improved energy yield of 20%. Hence, the series-parallel network's net energy output, shown in **Fig. 8a**, saves nearly thrice the parallel's to the SWRO plant (~9% of the SEC), yet it requires five times more RED modules, that would increase capital investment and operational expenses of the installation accordingly.

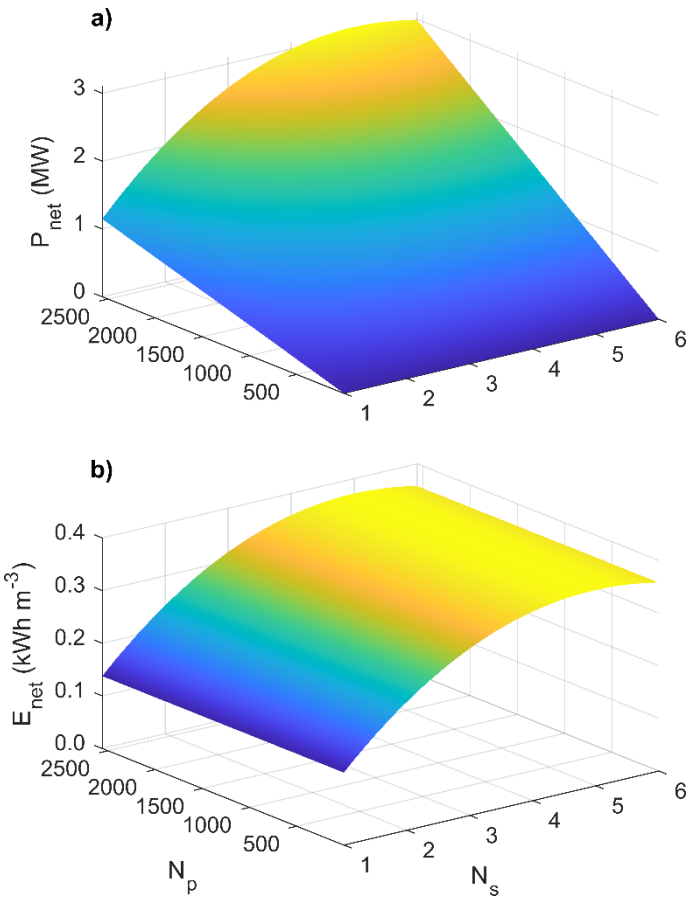

Figure 8. SGE-RED plant layouts: a) net power and b) net specific energy output of the SGE-RED plant according to the number of parallel N_p and series N_s units installed.

Overall these findings reveal the huge potential of RED technology to harvest SGE from effluents of energy-intensive processes as SWRO desalination plants, but at the same time underline the need of carrying out a detailed optimization, not only of the RED coupled process's layout but also the operational conditions of each RED stack in the plant to maximize the power density and energy efficiency of the whole system while minimizing the required capital investment and operational expenses.

4. CONCLUSIONS

This study deals with the evaluation of an up-scaled SGE-RED system's energy generation integrated into a SWRO desalination plant. An updated modelling tool was used to predict the performance and to estimate the potential power and energy output of the system in the different scenarios.

First, we conducted a parametric evaluation of feed solutions' concentrations, feed's flow rate, and the combined effect of feed's temperature and diluate's feed flow rate to determine the optimal operating conditions of the stand-alone RED unit. The RED unit operation with larger concentration gradients keeping diluate's concentrations above 0.017 M and concentrate to diluate linear velocity ratio to v_{HC}:v_{LC} ~0.6 provides enhanced net power densities. The findings also revealed that RED performance, as well as diluate's linear velocity, were greatly affected by inlet stream's temperature. The net power density almost doubles and the optimum diluate's linear velocity increases when the feed solutions are warmed up from 10°C to 30°C due to the higher mobility of ions and changes in the rheological properties (lower viscosity) of the streams with temperature.

Subsequently, we estimated the maximum SGE available and the net energy recovery and net power output of the SGE-RED plant in six SWRO desalination plants distributed worldwide, –with brine effluent's concentration, temperature, and volume ranges of 1.0–1.5 M NaCl, 18–31°C, and 0.8–1.4 m^3 per m^3 of desalted water, respectively– highlighting the merits of this tool to assist the selection of the most favorable scenarios for SGE-RED implementation.

Finally, we examined how different SGE-RED plant's layouts in Barcelona's SWRO desalination plant, selected according to the power and energy output potential and source availability, could improve the overall power output and energy recovery of the RED system. Although the addition of RED units in parallel results in greater power output (P_{net} = 1.15 MW), only a small fraction of SGE is converted into useful work (7%). The energy yield can be increased by 20% and the power output tripled implementing a series-parallel arrangement in the SGE-RED plant at the expense of five times more RED modules, that would raise the capital investment and operational expenses accordingly.

The energy efficiency and power density are mutually bound by a trade-off relationship. An actual full-scale SGE-RED plant will require to reconcile the two conflicting metrics and reach an optimized balance of high efficiency (energy yield) and large power density. These findings reveal the huge potential of RED technology to harvest SGE from waste streams in SWRO plants, but also reveal the need of a systematic evaluation through optimization of the hybrid process configuration at plant's scale as well as the RED unit's scale to maximize the net power density and energy yield of the system while minimizing capital outlay and operational expenses.

ACKNOWLEDGEMENTS

This work was supported by the Community of Cantabria - Regional Plan through the project Gradisal (RM16-XX-046-SODERCAN/FEDER); and the Spanish Ministry of Science, Innovation and Universities (RTI2018-093310-B-I00 and CTM2017-87850-R). Carolina Tristán is supported by the Spanish Ministry of Science, Innovation and Universities (FPI grant PRE2018-086454).

REFERENCES

[1] UNESCO, UN-Water, 2020: United Nations World Water Development Report 2020: Water and Climate Change, UNESCO, Paris, 2020. https://unesdoc.unesco.org/ark:/48223/pf0000372985.locale=en.

[2] GWI, IDA, IDA Water Security Handbook 2018 - 2019, Media Analytics Ltd., UK, 2018.

[3] IEA, WEO-2016 Special Report: Water-Energy Nexus, Paris, 2016. doi:10.1021/es2016632.

[4] N.Y. Yip, D. Brogioli, H.V.M. Hamelers, K. Nijmeijer, Salinity gradients for sustainable energy: Primer, progress, and prospects, Environ. Sci. Technol. 50 (2016) 12072–12094. doi:10.1021/acs.est.6b03448.

[5] B.E. Logan, M. Elimelech, Membrane-based processes for sustainable power generation using water, Nature. 488 (2012) 313–319. doi:10.1038/nature11477.

[6] H. Tian, Y. Wang, Y. Pei, J.C. Crittenden, Unique applications and improvements of reverse electrodialysis: A review and outlook, Appl. Energy. 262 (2020) 114482. doi:10.1016/J.APENERGY.2019.114482.

[7] R.A. Tufa, S. Pawlowski, J. Veerman, K. Bouzek, E. Fontananova, G. di Profio,

S. Velizarov, J. Goulão Crespo, K. Nijmeijer, E. Curcio, Progress and prospects in reverse electrodialysis for salinity gradient energy conversion and storage, Appl. Energy. 225 (2018) 290–331. doi:10.1016/J.APENERGY.2018.04.111.

[8] Y. Mei, C.Y. Tang, Recent developments and future perspectives of reverse electrodialysis technology: A review, Desalination. 425 (2017) 156–174. doi:10.1016/j.desal.2017.10.021.

[9] R.E. Pattle, Production of Electric Power by mixing Fresh and Salt Water in the Hydroelectric Pile, Nature. 174 (1954) 660–660. doi:10.1038/174660a0.

[10] A. Daniilidis, D.A. Vermaas, R. Herber, K. Nijmeijer, Experimentally obtainable energy from mixing river water, seawater or brines with reverse electrodialysis, Renew. Energy. 64 (2014) 123–131. doi:10.1016/j.renene.2013.11.001.

[11] J.W. Post, H.V.M. Hamelers, C.J.N. Buisman, Energy Recovery from Controlled Mixing Salt and Fresh Water with a Reverse Electrodialysis System, Environ. Sci. Technol. 42 (2008) 5785–5790. doi:10.1021/es8004317.

[12] J. Veerman, R.M. de Jong, M. Saakes, S.J. Metz, G.J. Harmsen, Reverse electrodialysis: Comparison of six commercial membrane pairs on the thermodynamic efficiency and power density, J. Memb. Sci. 343 (2009) 7–15. doi:10.1016/J.MEMSCI.2009.05.047.

[13] J.-Y. Nam, K.-S. Hwang, H.-C. Kim, H. Jeong, H. Kim, E. Jwa, S. Yang, J. Choi, C.-S. Kim, J.-H. Han, N. Jeong, Assessing the behavior of the feed-water constituents of a pilot-scale 1000-cell-pair reverse electrodialysis with seawater and municipal wastewater effluent, Water Res. 148 (2019) 261–271. doi:10.1016/J.WATRES.2018.10.054.

[14] J. Veerman, M. Saakes, S.J. Metz, G.J. Harmsen, Electrical Power from Sea and River Water by Reverse Electrodialysis: A First Step from the Laboratory to a Real Power Plant, Environ. Sci. Technol. 44 (2010) 9207–9212. doi:10.1021/es1009345.

[15] J. Veerman, M. Saakes, S.J. Metz, G.J. Harmsen, Reverse electrodialysis: Performance of a stack with 50 cells on the mixing of sea and river water, J. Memb. Sci. 327 (2009) 136–144. doi:10.1016/j.memsci.2008.11.015.

[16] J. Moreno, S. Grasman, R. van Engelen, K. Nijmeijer, Upscaling Reverse Electrodialysis, Environ. Sci. Technol. 52 (2018) 10856–10863. doi:10.1021/acs.est.8b01886.

[17] J.W. Post, C.H. Goeting, J. Valk, S. Goinga, J. Veerman, H.V.M. Hamelers, P.J.F.M. Hack, Towards implementation of reverse electrodialysis for power generation from salinity gradients, Desalin. Water Treat. 16 (2010) 182–193. doi:10.5004/dwt.2010.1093.

[18] M. Tedesco, C. Scalici, D. Vaccari, A. Cipollina, A. Tamburini, G. Micale, Performance of the first reverse electrodialysis pilot plant for power production from saline waters and concentrated brines, J. Memb. Sci. 500 (2016) 33–45. doi:10.1016/j.memsci.2015.10.057.

[19] M. Tedesco, A. Cipollina, A. Tamburini, G. Micale, Towards 1 kW power production in a reverse electrodialysis pilot plant with saline waters and concentrated brines, J. Memb. Sci. 522 (2017) 226–236. doi:10.1016/j.memsci.2016.09.015.

[20] M. Vanoppen, S. Derese, A. Bakelants, A.R.D. Verliefde, Reduction of specific energy demand of seawater RO by osmotic dilution/osmotic energy recovery -

realistic modelling approach, Desalin. Environ. Clean Water Energy. (2014) 23–24.

[21] Y. Mei, C.Y. Tang, Co-locating reverse electrodialysis with reverse osmosis desalination: Synergies and implications, J. Memb. Sci. 539 (2017) 305–312. doi:10.1016/j.memsci.2017.06.014.

[22] E. Brauns, An alternative hybrid concept combining seawater desalination, solar energy and reverse electrodialysis for a sustainable production of sweet water and electrical energy, Desalin. Water Treat. 13 (2010) 53–62. doi:10.5004/dwt.2010.1090.

[23] W. Li, W.B. Krantz, E.R. Cornelissen, J.W. Post, A.R.D. Verliefde, C.Y. Tang, A novel hybrid process of reverse electrodialysis and reverse osmosis for low energy seawater desalination and brine management, Appl. Energy. 104 (2013) 592–602. doi:10.1016/j.apenergy.2012.11.064.

[24] K. Kwon, J. Han, B.H. Park, Y. Shin, D. Kim, Brine recovery using reverse electrodialysis in membrane-based desalination processes, Desalination. 362 (2015) 1–10. doi:10.1016/j.desal.2015.01.047.

[25] S. Mehdizadeh, M. Yasukawa, M. Kuno, Y. Kawabata, M. Higa, Evaluation of energy harvesting from discharged solutions in a salt production plant by reverse electrodialysis (RED), Desalination. 467 (2019) 95–102. doi:10.1016/J.DESAL.2019.04.007.

[26] J. Choi, Y. Oh, S. Chae, S. Hong, Membrane capacitive deionization-reverse electrodialysis hybrid system for improving energy efficiency of reverse osmosis seawater desalination, Desalination. 462 (2019) 19–28. doi:10.1016/J.DESAL.2019.04.003.

[27] L. Gómez-Coma, V.M. Ortiz-Martínez, M. Fallanza, A. Ortiz, R. Ibañez, I. Ortiz, Blue energy for sustainable water reclamation in WWTPs, J. Water Process Eng. 33 (2020) 101020. doi:10.1016/J.JWPE.2019.101020.

[28] J. Luque Di Salvo, A. Cosenza, A. Tamburini, G. Micale, A. Cipollina, Long-run operation of a reverse electrodialysis system fed with wastewaters, J. Environ. Manage. 217 (2018) 871–887. doi:10.1016/j.jenvman.2018.03.110.

[29] S. Mehdizadeh, M. Yasukawa, T. Suzuki, M. Higa, Reverse electrodialysis for power generation using seawater/municipal wastewater: Effect of coagulation pretreatment, Desalination. 481 (2020) 114356. doi:10.1016/J.DESAL.2020.114356.

[30] R.A. Tufa, E. Curcio, W. van Baak, J. Veerman, S. Grasman, E. Fontananova, G. Di Profio, Potential of brackish water and brine for energy generation by salinity gradient power-reverse electrodialysis (SGP-RE), RSC Adv. 4 (2014) 42617–42623. doi:10.1039/C4RA05968A.

[31] M. Tedesco, A. Cipollina, A. Tamburini, W. van Baak, G. Micale, Modelling the Reverse ElectroDialysis process with seawater and concentrated brines, Desalin. Water Treat. 49 (2012) 404–424. doi:10.1080/19443994.2012.699355.

[32] G.Z. Ramon, B.J. Feinberg, Z.L.T. Yu, E.M. V. Hoek, Membrane-based production of salinity-gradient power, Energy Environ. Sci. 4 (2011) 4423–4434. doi:10.1039/c1ee01913a.

[33] R.A. Tufa, E. Curcio, E. Brauns, W. van Baak, E. Fontananova, G. Di Profio, Membrane Distillation and Reverse Electrodialysis for Near-Zero Liquid Discharge and low energy seawater desalination, J. Memb. Sci. 496 (2015) 325–333. doi:10.1016/J.MEMSCI.2015.09.008.

[34] R. Ortiz-Imedio, L. Gomez-Coma, M. Fallanza, A. Ortiz, R. Ibañez, I. Ortiz, Comparative performance of Salinity Gradient Power-Reverse Electrodialysis under different operating conditions, Desalination. 457 (2019) 8–21. doi:10.1016/J.DESAL.2019.01.005.

[35] V.M. Ortiz-Martínez, L. Gómez-Coma, C. Tristán, G. Pérez, M. Fallanza, A. Ortiz, R. Ibañez, I. Ortiz, A comprehensive study on the effects of operation variables on reverse electrodialysis performance, Desalination. 482 (2020) 114389. doi:10.1016/J.DESAL.2020.114389.

[36] A. Campione, L. Gurreri, M. Ciofalo, G. Micale, A. Tamburini, A. Cipollina, Electrodialysis for water desalination: A critical assessment of recent developments on process fundamentals, models and applications, Desalination. 434 (2018) 121–160. doi:10.1016/J.DESAL.2017.12.044.

[37] R.E. Lacey, Energy by reverse electrodialysis, Ocean Eng. 7 (1980) 1–47. doi:10.1016/0029-8018(80)90030-X.

[38] E. Brauns, Salinity gradient power by reverse electrodialysis: effect of model parameters on electrical power output, Desalination. 237 (2009) 378–391. doi:10.1016/j.desal.2008.10.003.

[39] J. Veerman, M. Saakes, S.J. Metz, G.J. Harmsen, Reverse electrodialysis: A validated process model for design and optimization, Chem. Eng. J. 166 (2011) 256–268. doi:10.1016/j.cej.2010.10.071.

[40] M. Tedesco, A. Cipollina, A. Tamburini, I.D.L. Bogle, G. Micale, A simulation tool for analysis and design of reverse electrodialysis using concentrated brines, Chem. Eng. Res. Des. 93 (2015) 441–456. doi:10.1016/j.cherd.2014.05.009.

[41] M. Tedesco, P. Mazzola, A. Tamburini, G. Micale, I.D.L. Bogle, M. Papapetrou, A. Cipollina, Analysis and simulation of scale-up potentials in reverse electrodialysis, Desalin. Water Treat. 55 (2015) 3391–3403. doi:10.1080/19443994.2014.947781.

[42] S. Pawlowski, V. Geraldes, J.G. Crespo, S. Velizarov, Computational fluid dynamics (CFD) assisted analysis of profiled membranes performance in reverse electrodialysis, J. Memb. Sci. 502 (2016) 179–190. doi:10.1016/j.memsci.2015.11.031.

[43] M.L. La Cerva, M. Di Liberto, L. Gurreri, A. Tamburini, A. Cipollina, G. Micale, M. Ciofalo, Coupling CFD with a one-dimensional model to predict the performance of reverse electrodialysis stacks, J. Memb. Sci. 541 (2017) 595–610. doi:10.1016/j.memsci.2017.07.030.

[44] B. Ortega-Delgado, F. Giacalone, A. Cipollina, M. Papapetrou, G. Kosmadakis, A. Tamburini, G. Micale, Boosting the performance of a Reverse Electrodialysis – Multi-Effect Distillation Heat Engine by novel solutions and operating conditions, Appl. Energy. 253 (2019) 113489. doi:10.1016/J.APENERGY.2019.113489.

[45] L. Gómez-Coma, V.M. Ortiz-Martínez, J. Carmona, L. Palacio, P. Prádanos, M. Fallanza, A. Ortiz, R. Ibañez, I. Ortiz, Modeling the influence of divalent ions on membrane resistance and electric power in reverse electrodialysis, J. Memb. Sci. 592 (2019) 117385. doi:10.1016/J.MEMSCI.2019.117385.

[46] A. Culcasi, L. Gurreri, A. Zaffora, A. Cosenza, A. Tamburini, A. Cipollina, G. Micale, Ionic shortcut currents via manifolds in reverse electrodialysis stacks, Desalination. 485 (2020) 114450. doi:10.1016/J.DESAL.2020.114450.

[47] Z. Jalili, J.G. Pharoah, O.S. Burheim, K.E. Einarsrud, Temperature and velocity effects on mass and momentum transport in spacer-filled channels for reverse electrodialysis: A numerical study, Energies. 11 (2018). doi:10.3390/en11082028.

[48] J. Hu, S. Xu, X. Wu, D. Wu, D. Jin, P. Wang, Q. Leng, Theoretical simulation and evaluation for the performance of the hybrid multi-effect distillation—reverse electrodialysis power generation system, Desalination. 443 (2018) 172–183. doi:10.1016/J.DESAL.2018.06.001.

[49] J. Hu, S. Xu, X. Wu, D. Wu, D. Jin, P. Wang, Q. Leng, Multi-stage reverse electrodialysis: Strategies to harvest salinity gradient energy, Energy Convers. Manag. 183 (2019) 803–815. doi:10.1016/J.ENCONMAN.2018.11.032.

[50] J. Hu, S. Xu, X. Wu, S. Wang, X. Zhang, S. Yang, R. Xi, D. Wu, L. Xu, Experimental investigation on the performance of series control multi-stage reverse electrodialysis, Energy Convers. Manag. 204 (2020) 112284. doi:10.1016/J.ENCONMAN.2019.112284.

[51] Aspentech, Aspen Plus, (2019).

[52] Aspentech, Aspen Custom Modeler, (2019).

[53] S. Mehdizadeh, M. Yasukawa, T. Abo, M. Kuno, Y. Noguchi, M. Higa, The Effect of Feed Solution Temperature on the Power Output Performance of a Pilot-Scale Reverse Electrodialysis (RED) System with Different Intermediate Distance, Membranes (Basel). 9 (2019) 73. doi:10.3390/membranes9060073.

[54] J. Kim, K. Park, D.R. Yang, S. Hong, A comprehensive review of energy consumption of seawater reverse osmosis desalination plants, Appl. Energy. 254

(2019) 113652. doi:10.1016/J.APENERGY.2019.113652.

[55] M.A. Sanz, C. Miguel, The role of SWRO Barcelona-Llobregat Plant in the water supply system of Barcelona Area, Desalin. Water Treat. 51 (2013) 111–123. doi:10.1080/19443994.2012.699250.

[56] K.L. Petersen, N. Heck, B.G. Reguero, D. Potts, A. Hovagimian, A. Paytan, K. Lykkebo Petersen, N. Heck, B. G. Reguero, D. Potts, A. Hovagimian, A. Paytan, Biological and Physical Effects of Brine Discharge from the Carlsbad Desalination Plant and Implications for Future Desalination Plant Constructions, Water. 11 (2019) 208. doi:10.3390/w11020208.

[57] N. Fujiwara, H. Matsuyama, High recovery system in seawater reverse osmosis plants, J. Appl. Polym. Sci. 108 (2008) 3403–3410. doi:10.1002/app.27943.

[58] M. Sekino, A. Kumano, N. Fujiwara, Expanding Technology of Seawater Desalination Membrane, Bull. Soc. Sea Water Sci. Japan. 60 (2006) 408–414. doi:10.11457/swsj1965.60.408.

[59] F. Giacalone, F. Vassallo, L. Griffin, M.C. Ferrari, G. Micale, F. Scargiali, A. Tamburini, A. Cipollina, Thermolytic reverse electrodialysis heat engine: model development, integration and performance analysis, Energy Convers. Manag. 189 (2019) 1–13. doi:10.1016/J.ENCONMAN.2019.03.045.

[60] F. Giacalone, P. Catrini, A. Tamburini, A. Cipollina, A. Piacentino, G. Micale, Exergy analysis of reverse electrodialysis, Energy Convers. Manag. 164 (2018) 588–602. doi:10.1016/j.enconman.2018.03.014.

[61] K.W. Krakhella, R. Bock, O.S. Burheim, F. Seland, K.E. Einarsrud, Heat to H2: Using Waste Heat for Hydrogen Production through Reverse Electrodialysis,

Energies. 12 (2019) 3428. doi:10.3390/en12183428.